Adaptive Virtual Synchronous Generator Considering Converter and Storage Capacity Limits

Junru Chen, *Member, IEEE*, Muyang Liu, *Member*, *IEEE*, Federico Milano*, Fellow, IEEE,* Terence O'Donnell, *Senior Member, IEEE*

***Abstract*—Virtual Synchronous Generator (VSG) control has been proposed as a means to control voltage source converter interfaced generations and storage to retain the dynamics of conventional synchronous generator. The storage is used to provide the inertia power and droop power in the VSG control to improve the frequency stability. Since the parameter in VSG can be varied, then it can be tuned to be adaptive in order to achieve an optimal response to the grid frequency. However, the storage cannot provide infinite power and the converter has a strict power limitation on its capacity. The adaptive VSG control should consider these limitations, which has not been concerned before. This paper proposes an adaptive VSG control aimed at obtaining the optimal grid supporting services during frequency transients, accounting for converter and storage capacity limitations. The proposed control has been validated via hardware-in-the-loop testing. It is then implemented in storage co-located with wind farms in a modified IEEE 39-bus system, the results show that the proposed control stabilizes the system faster and has better cooperation with other VSGs under considerations of storage and converter limits.**

***Index Terms*—virtual synchronous generator, adaptive control, converter capacity, state of storage**

I. Introduction

Increased generation from renewable energy sources, such as wind turbines and photovoltaics, leads to the situation where maintaining the balance between supply and demand becomes more difficult, due to the stochastic nature of the supply. At the same time renewable generation lacks intrinsic inertia, so that supply demand imbalance can lead to higher rates of change of frequency (RoCoF) [1][2]. In this context, energy storage systems (ESS) can be used to quickly compensate the power mismatch between the supply and demand and improve the system stability [2]. During transients, the ESS can be controlled to emulate the inertia (called virtual inertia) response and provide a droop response and hence improve frequency nadir and frequency deviation.

The implementation of the virtual inertia in the ESS can be broadly classified into two types: an extra power response based on measured frequency deviation implemented in a grid-feeding converter [3] or inertial emulation through virtual synchronous generator control [4-6] implemented on grid-forming converters. The grid-feeding converter controls the power directly [7], so that its power output can be linked to the measured grid frequency deviation and RoCoF usually detected by the phase locked loop (PLL) [8-10]. The power output of the ESS should also respect the ESS state of charge (SoC) limits in order to maintain a healthy operation of the storage [11]. For example, a healthy SoC of battery storage should be typically be in a range of 20% to 80% for the sake of a longer lifetime and reliability [12]. In a 100% non-synchronous system, grid-forming converters are a must-have in the system in order to take over the responsibilities of the synchronous generator to establish the voltage and form the grid [13]. For example, reference [14][15] claims that at least 30% of the generators in such a system should be grid-forming to achieve a stable system. Grid forming converter controls can be implemented by various methods. On such methods is Virtual synchronous generator control (VSG) which mimics the dynamics of the SG in order to achieve self-synchronizing and more importantly, provide the inertia response to the system [16-18].

In principle, the VSG control is designed to mimic the synchronous generator (SG) behavior, including the swing equation and turbine governor for the P-ω regulation, automatic voltage regulation for Q-V regulation and stator impedance emulated through virtual impedance [16-22]. Reference [23] compares VSG versus SG performance and concludes that in terms of these aspects the VSG and SG performance in the system can be identical. However, a key difference between the SG and the VSG is the fact that the VSG is a power electronics device with the possibility to change its response through changing its control settings. Thus, for example, with proper control settings, it can achieve better performance in terms of frequency oscillation suppression than the synchronous generator. Based on small-signal analysis [24], variable and adaptive inertia and damping settings [25-31] can be selected for the VSG. For example, reference [25] has proposed an alternating inertia setting during VSG acceleration and deceleration. References [26][27] further develops this method by considering the damping term. Reference [28][29][31] proposes an algorithm to optimize the inertia and damping to minimize both amplitude and rate of change of frequency variations, whereas reference [30] has proposed adaptive inertia and damping for fault ride-through. However, these works are

This work was supported by the Science Foundation Ireland (SFI) under the projects ESIPP, Grant No. SFI/15/SPP/E3125, and AMPSAS, Grant No. SFI/15/IA/3074.

J. Chen, M. Liu, F. Milano and T. O'Donnell are with the Electrical Engineering Department, University College Dublin, Dublin 4, Ireland (e-mail: junru.chen.1@ucdconnect.ie, terence.odonnell@ucd.ie)

based on the assumption that the ESS is ideal with infinite energy and the converter of the ESS has no power limit.

The grid-forming converter controls the voltage directly, and the power is the consequence of the voltage difference between the converter and the grid [7]. The active power control in the grid-forming converter, especially using VSG control, is not instantaneous and is delayed by the inertia and damping effects. Even if the maximum power reference is limited, the transient output power overshoot can be excessive, especially for a high inertia setting, which can lead to converter overload. Moreover, the power response should respect the SoC limits of the storage. Thus, the choice of VSG parameters is constrained by the capacity of the converter and the storage. None of the previous works have considered the power capacity and SoC constraints of the VSG energy storage, and this paper attempts to fill this gap. Therefore, the contribution of this paper is to propose an adaptive VSG control which can account for the ESS limitations, achieving an improved system frequency stability and an improved co-ordination between the ESS in the system.

This paper first reviews VSG model in Section II. From the analysis of VSG parametric effects, the proposed adaptive control is introduced in section III. In Section IV, the hardware in the loop experiment is used to compare the proposed method with the conventional VSG method. The system level comparison is analyzed in Section V using IEEE 39-bus system.

II. Virtual Synchronous Generator

This section reviews the VSG equations and deduces its transfer function relating the inputs to outputs.

A. VSG Model

It is assumed that VSG control is implemented into the grid-tied inverter, of which the DC bus is interfaced with renewable generation and/or storage. The voltage source VSG directly controls the output voltage through the P-ω and Q-V control. The power flow is determined by the potential difference between the VSG and grid. The VSG function and modeling have been previously detailed in [17-19] and here we quickly review the analysis and focus on its core function.

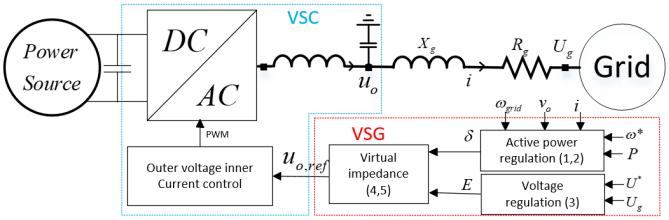

Fig. 1. VSG control structure

Fig. 1 illustrates the structure of the VSG. The VSG control measures the real power P and through the swing equation (1) determines the VSG frequency ω_{VSG} and angle δ relative to the grid voltage. Here the grid voltage is taken as the reference, i.e., $\overrightarrow{u_g} = U_g\angle 0°$, where J is inertia, D is damping, K_d is droop gain, ω^* is reference frequency and P^* is VSG reference active power which may come from a renewable generation source. The measured reactive power Q, through Q-V droop with gain K_q , determines the electric potential amplitude E as (3a), where U^* is voltage reference, Q^* is reactive power reference, which could include additional V-Q compensation (3b). The electric potential $\vec{e}$ is determined as (4). The virtual impedance $R_v + jX_v$ is assumed to connect to the grid impedance $R_g + jX_g$ in series. Since the virtual impedance only exists in the control loop, the actual VSG output voltage is the voltage after the virtual impedance as shown in (5a). Compared with the VSG control, the VSC control is much faster and can be neglected [32] (i.e. $u_o = u_{o,ref}$). The power flow between the electric potential $\vec{e}$ and grid voltage $\overrightarrow{u_g}$ is presented as (6) and (7), and the VSG output power can be computed as (8) (9). Therefore, equations (1~9) define the model of the VSG.

$$\begin{cases} J\dfrac{d\Delta\omega_{VSG}}{dt} = P^* + K_d(\omega_g - \omega^*) - P - D\Delta\omega_{VSG} \\ \Delta\omega_{VSG} = \omega_{VSG} - \omega_g \end{cases} \quad (1)$$

$$\dot{\delta} = \Delta\omega_{VSG} \quad (2)$$

$$E = U^* + K_q(Q^* - Q) \quad (3a)$$

$$Q^* = \mathrm{Q}_0 + K_v(U^* - U_g) \quad (3b)$$

$$\vec{\mathrm{e}} = e_d + je_q = E\cos\delta + jE\sin\delta \quad (4)$$

$$\overrightarrow{u_o} = \vec{e} - (R_v + jX_v)\vec{\mathrm{i}} \quad (5a)$$

$$\begin{cases} u_{od} = E\cos\delta - i_d R_v + i_q X_v \\ u_{oq} = E\sin\delta - i_d X_v - i_q R_v \end{cases} \quad (5b)$$

$$\begin{cases} R = R_v + R_g \\ X = X_v + X_g = \omega_{VSG}L_v + \omega_g L_v \end{cases} \quad (6)$$

$$\vec{\mathrm{i}} = i_d + ji_q = \frac{\vec{\mathrm{e}} - \overrightarrow{u_g}}{R + jX} \quad (7a)$$

$$\begin{cases} i_d = \dfrac{R}{R^2+X^2}(e_d - u_{gd}) + \dfrac{X}{R^2+X^2}(e_q - u_{gq}) \\ i_q = -\dfrac{X}{R^2+X^2}(e_d - u_{gd}) + \dfrac{R}{R^2+X^2}(e_q - u_{gq}) \end{cases} \quad (7b)$$

$$P = \frac{3}{2}(u_{od}i_d + u_{oq}i_q) \quad (8)$$

$$Q = \frac{3}{2}(-u_{od}i_q + u_{oq}i_d) \quad (9)$$

B. Small-Signal Model

In steady state, the value of the grid voltage, virtual impedance and line impedance are constant, and the electric potential is E_0 and its phase is δ_0. Assuming ΔE and $\Delta\delta$ are the small-signal perturbation for the electric potential and its phase, substituting $E_0 + \Delta E$ and $\delta_0 + \Delta\delta$ into (4,5,7) and obtaining output current $i_d + \Delta i_d + j(i_q + \Delta i_q)$ and voltage $u_{od} + \Delta u_{od} + j(u_{oq} + \Delta u_{oq})$, and then substituting the resultant into (8) and (9) respectively, we obtain the small-signal gain of output power to the phase angle ($H_{dP/d\delta}$, $H_{dQ/d\delta}$) and potential ($H_{dP/dE}$, $H_{dQ/dE}$) respectively [33].

$$H_{dP/d\delta} = \frac{\Delta P}{\Delta\delta} = \frac{3(E_0U_gR\sin\delta_0 + E_0U_gX\cos\delta_0)}{2(R^2+X^2)} - \frac{3(E_0U_gR^2R_v\sin\delta_0 + E_0U_gX^2R_v\cos\delta_0)}{(R^2+X^2)^2} \quad (10)$$

$$H_{dQ/d\delta} = \frac{\Delta Q}{\Delta\delta} = \frac{3(E_0U_gX\sin\delta_0 - E_0U_gR\cos\delta_0)}{2(R^2+X^2)} - \frac{3(E_0U_gR^2X_v\sin\delta_0 + E_0U_gX^2X_v\cos\delta_0)}{(R^2+X^2)^2} \quad (11)$$

$$H_{dP/dE} = \frac{\Delta P}{\Delta E} = \frac{3(2E_0R - U_gR\cos\delta_0 + U_gX\sin\delta_0)}{2(R^2+X^2)}$$

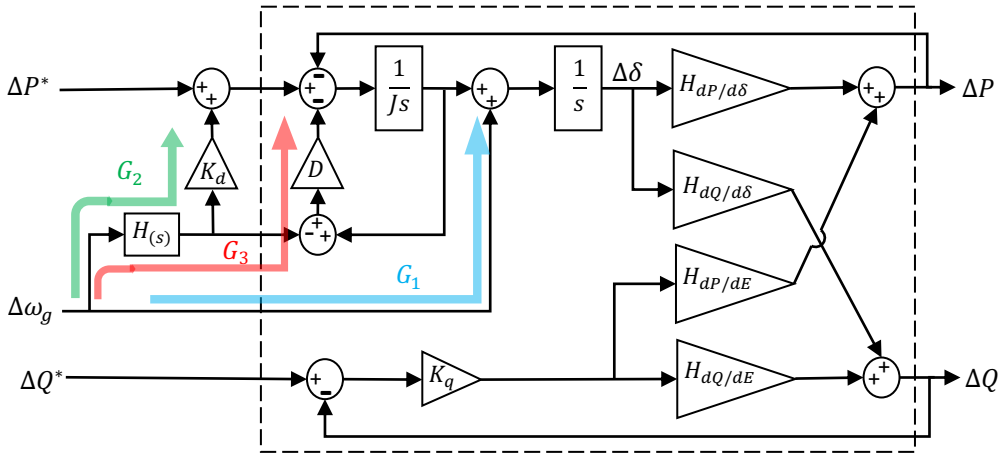

Fig. 2. VSG small-signal model diagram

$$+\frac{3(U_g X^2 R_v cos\delta_0 + U_g R^2 R_v cos\delta_0 - E_0 X^2 R_v - E_0 R^2 R_v)}{(R^2+X^2)^2} \quad (12)$$

$$H_{dQ/dE} = \frac{\Delta Q}{\Delta E} = \frac{3(2E_0 X - U_g X cos\delta_0 - U_g R sin\delta_0)}{2(R^2+X^2)}$$
$$+\frac{3(U_g X^2 X_v cos\delta_0 + U_g R^2 X_v cos\delta_0 - E_0 X^2 X_v - E_0 R^2 X_v)}{(R^2+X^2)^2} \quad (13)$$

Note, these gains ($H_{dP/d\delta}, H_{dQ/d\delta}, H_{dP/dE}, H_{dQ/dE}$) change with operating point and the value of these gains depends on the virtual impedance $R_v + jX_v$, line impedance $R_g + jX_g$, grid voltage U_g, initial electric potential E_0 and its phase δ_0.

Now considering the above relationships, the closed loop small-signal model diagram is shown in Fig. 2, where $H_{(s)}$ represents the PLL dynamics. Note, the grid synchronization of the VSG is achieved by the swing equation not the PLL, and hence the PLL dynamics do not affect the synchronization [37] or the VSG stability. The PLL is only used to detect the frequency deviation for the droop control, thus, for simplification, the PLL time constant is neglected, i.e. $H_{(s)} = 1$. Note, that in some VSG implementations [16,19], the damping and droop can be made the same in which case the PLL can be completely removed.

C. *Transfer functions*

The paper focuses on the active power compensation in response to the grid frequency, for which the transfer function in Fig. 2 contains three loops. The first loop G_1 represents the change in grid frequency which instantly changes the grid phase difference with the VSG resulting in the power change. In this loop, the damping term has a transient droop feature which adds power due to the transient frequency deviation between the VSG and grid. The second loop G_2 represents the droop power which adds to the power reference and is output via VSG generation. The third loop G_3 is used to cancel the droop effects of the damping term and ensure that the VSG frequency equals the grid frequency in steady state.

Defining $c_1 = H_{dP/d\delta} - H_{dQ/d\delta} H_{dP/dE} \frac{K_q}{1+K_q H_{dQ/dE}}$, is the gain of active power ΔP to phase $\Delta\delta$ change as shown in Fig. 2, which includes not only $H_{dP/d\delta}$, but also the phase effects on the reactive power which results in the reference electric potential change and which in turn influences the active power, i.e. $-H_{dQ/d\delta} H_{dP/dE} \frac{K_q}{1+K_q H_{dQ/dE}}$. Then the transfer functions, G_1, G_2, G_3, can be obtained as illustrated in Fig. 3.

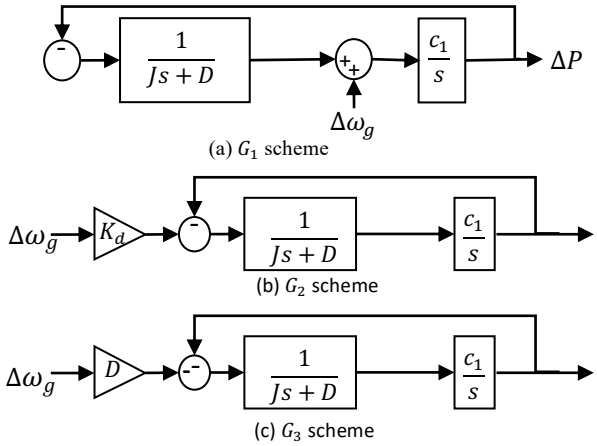

Fig. 3. Transfer functions showing the effect of a change in grid frequency on power output (a) G1 represents the effect of a change in grid frequency on power output through the inertial effect, (b) G2 represents the effect of a change in grid frequency on output power through the droop response (c) G3 represents the effect of a change in grid frequency on output power through the damping power.

$$G_1 = \frac{c_1(Js+D)}{Js^2+Ds+c_1} \quad (14)$$

$$G_2 = \frac{K_d c_1}{Js^2+Ds+c_1} \quad (15)$$

$$G_3 = -\frac{Dc_1}{Js^2+Ds+c_1} \quad (16)$$

Then grid frequency to output active power transfer function, G_{P_ω} is

$$G_{P\_\omega} = G_1 + G_2 + G_3 = \frac{c_1(Js+K_d)}{Js^2+Ds+c_1} \quad (17)$$

The transfer function (17) is second order. The damping associated with the transient response is an important characteristic with consequences for the converter and the grid. For example, in the case of a reference power change, the response should be overdamped (damping ratio greater than 1) in order to provide large damping and prevent oscillations. However, in the case of a grid frequency disturbance, the

response should be underdamped in order to provide a larger inertial response during the transient.

With respect to the step response of the system, the damping ratio ζ for G_{P_ω} can be obtained as:

$$\zeta = \frac{D}{2\sqrt{Jc_1}} \tag{18}$$

When ζ >1, the system is overdamped and the settling time can be calculated as (22).

$$t_s = \frac{8J}{D - \sqrt{D^2 - 4Jc_1}} \tag{19}$$

When ζ <1, the system is underdamped and gives rise to overshoot. The rise time, t_{p_ω} can be computed as (23) and overshoot PO_{P_ω} can be computed as (24),where $\omega_{P_\omega} = \sqrt{\frac{c_1}{J} - \frac{D^2}{4J^2}}$ and $a_{p_\omega} = \frac{D}{2J}$.

$$t_{p\omega} = \frac{\tan^{-1}\frac{\omega_{P_\omega}}{a_{P_\omega}} - \tan^{-1}\frac{K_d\omega_{P_\omega}}{K_d a_{P_\omega} - c_1}}{\omega_{P_\omega}} \tag{20}$$

$$PO_{P\_\omega} = \frac{c_1}{\omega_{P_f}} e^{-a_{p\omega}\cdot t}\sin\left(\omega_{P_\omega}\cdot t_{p_\omega}\right) + K_d(1 - e^{-a_{p\omega}\cdot t}\cdot \cdot\cos\left(\omega_{P_\omega}\cdot t_{p_\omega}\right) - \frac{a_{P\omega}}{\omega_{P_\omega}} e^{-a_{p\omega}\cdot t}\sin\left(\omega_{P_\omega}\cdot t_{p_\omega}\right)) \tag{21}$$

III. Adaptive Control

With the understanding of the effect of the parameters on the performance (18~21), the selection of the parameters can be optimized. Ideally, in steady state, the VSG should achieve zero steady-state error on reference tracking or accurate power sharing, and if connected to a variable renewable generation source, large damping will contribute to smooth the power output and maintain stability. However, during a transient triggered by a grid disturbance, it would be preferable for the VSG to rapidly provide a large inertial response in order to improve the system frequency stability in terms of frequency nadir and rate of change of frequency (RoCoF). Considering these requirements, the adaptive VSG control is proposed in this section.

The choice of adaptive parameters is considered to be used to not only stabilize the system but also limit the converter power flow. The critical parameters for VSG response to a frequency transient are damping ratio ζ (18), settling time t_s (19) or rise time $t_{p\omega}$ (20) and overshoot PO_{P_ω} (21). All of these terms are related to the gains $H_{dP/d\delta}, H_{dQ/d\delta}, H_{dP/dE}, H_{dQ/dE}$, damping/droop gain K_d and inertia J.

According to the grid code [34], for normal stable operation (we defined as steady-state mode), the frequency deviation band is ±0.2 Hz (±0.004 pu) while the RoCoF band is ±0.2 Hz/s. During transients, according to [26][27], the VSG response is divided into acceleration and deceleration of absolute frequency deviation. In acceleration, the virtual inertia should be larger in order to provide more inertia to system, while in deceleration, the damping should be larger and virtual inertia should be smaller in order to reduce the oscillation. However, considering the converter capacity and stability, the damping and virtual inertia are constrained.

A. Adaptive P-ω droop

In [34], the P-ω droop is required to be set as 4%, i.e. convert maximum reserve power for 4% frequency deviation. If the storage shares the converter with a DC renewable source, the maximum reserve power is limited by the converter capacity S and renewable power set point. Therefore, the nominal droop for frequency reduction and frequency increase is different as indicated in (22).

$$K_{d,0} = \begin{cases} (P_{max} - P^*)/0.04\omega^*, & \omega_{VSG} \le \omega^* \\ (P_{max} + P^*)/0.04\omega^*, & \omega_{VSG} > \omega^* \end{cases} \tag{22}$$

Where $P_{max} = \sqrt{S^2 - Q^*}$ is the maximum active power.

However, (22) is for normal operation with sufficient storage energy reserve. When the SoC is low, with a nominal droop gain given by (22), the storage may not have sufficient remaining capacity to provide the droop power with the possibility to suddenly lose the droop power, and adversely affect the system frequency response. In this case, the choice of K_d should be coordinated with the storage SoC and re-scheduling of the active power sharing. Hence, we use $K_{d,max}$ to constrain real power droop. Considering the unit commitment, the re-schedule interval is T_p (e.g. 20 min) [34]. The storage droop should cover this time period. Fig. 4 illustrates this process after the contingency, where E_s is the storage energy capacity and t is the accumulated time for the transients, with t0 being the time at the instant of the contingency or the detected frequency change, t1 is the settling time of the VSG, or the end time of the inertia response. Accordingly, SOC_{t0} is the initial SoC value at t0. The energy taken from the ESS until steady state is $\int_{t0}^{t1}(P - P^*)dt$. After this point, the power is used for the droop compensation. If the SoC of the ESS is low, a constant droop gain K_d may result in a sudden loss of the power, before the end of the time period, as shown by the solid line, while an adaptive gain linked to the SoC can ensure an uninterrupted power supply until the next system re-scheduling at T_p as indicated by the dashed line. The energy used during this period is the summation of the energy for inertia response during transient (t0-t1) and for droop compensation during steady state (t1-T_p) as computed in (23).

$$\begin{cases} \int_{t1}^{T_p} K_{d,max}(\omega^* - \omega_{VSG})dt = (SOC_{t0} - SOC_{min}) * E_s - \int_{t0}^{t1}(P - P^*)dt, \\ \qquad , \omega_{VSG} < \omega^* \\ \int_{t1}^{T_p} K_{d,max}(\omega_{VSG} - \omega^*)\,dt = (SOC_{max} - SOC_{t0}) * E_s - \int_{t0}^{t1}(P - P^*)dt, \\ \qquad , \omega_{VSG} > \omega^* \end{cases} \tag{23}$$

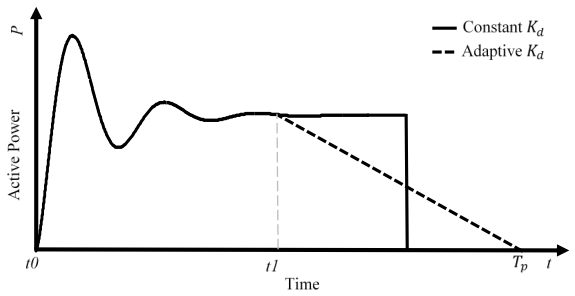

Fig. 4. The adaptive VSG control scheme

Solving (23) could obtain the $K_{d,max}$ as (24). Note, t re-sets at the beginning of each unit commitment. ω_{VSG} is the VSG frequency obtained from the control loop.

$$K_{d,max} = \begin{cases} [(SOC_{t0} - SOC_{min})E_s - \int_{t0}^{t}(P - P^*)\,dt]/[(T_p - t)(\omega^* - \omega_{VSG})], \\ \qquad , \omega_{VSG} < \omega^* \\ [(SOC_{max} - SOC_{t0})E_s - \int_{t0}^{t}(P - P^*)dt]/[(T_p - t)(\omega_{VSG} - \omega^*)], \\ \qquad , \omega^* < \omega_{VSG} \end{cases} \quad (24)$$

According to this approach, a low SoC storage limits its frequency to power support, and the high SoC storage should increase its frequency support capability by the means of droop gain increase. $K_{d,max}$ provides the upper limit on the droop gain. Reference [26] has proposed adapting droop gain with time according to the frequency deviation with time. This method could be used for the energy storage for active power re-sharing in order to alleviate the frequency deviation attributed to some storage being offline as indicated in (25).

$$K_d = K_{d,0} + n_d|\Delta\omega_{VSG}|, K_{d,min} \le K_{d,0} \le K_{d,max} \quad (25)$$

Where $\Delta\omega_{VSG} = \omega^* - \omega_{VSG}$; n_d is a coefficient for droop K_d, where n_d decreases when the number of adaptive VSG in the system is increased. Note $K_{d,min} = 0$, if using a separate droop and damping gain; $K_{d,min} = D_{min}$, if using a combined droop and damping gain for a sufficient damping as computed in (27). Note, in the latter case, when $K_{d,max} < K_{d,min}$, ($K_{d,max}$ is a function of SOC as computed in (24)) which means that the ESS is running out of the power and cannot maintain the stability, the PLL is used to take over the function of the synchronization to avoid the instability.

B. Adaptive damping

In terms of its effect on the damping ratio (18) the damping has an opposite effect to the inertia. In steady state, the damping should be large in order to damp the renewable generation and filter the VSG frequency oscillation. However, during transients, the damping would also have a droop effect as shown in Fig. 3 and in (14), especially in the combined droop and damping topology. From this point of view, D cannot be too large to avoid that the output power exceeds the rating of the converter. Therefore, the value should cover the steady-state frequency variance ± 0.02 Hz and ensure that the power change from transient damping is within the limit $P_{max} - P$ as (26), where P is the instantaneous power output from the VSG.

$$D_{max} = \frac{P_{max} - P}{0.02 \times 2\pi} \quad (26)$$

When the VSG is decelerating, the damping should be large in order to reduce the oscillation [26][27] but cannot be too large to avoid transient droop power exceeding the converter power limits. At the transition from the acceleration to deceleration, the output power will be at its maximum, due to the large inertia in acceleration. During the deceleration, the power would reduce from the maximum to the set value. Thus, D could be set as a droop during this process as indicated in (27), so that it is at a maximum at the start of deceleration and reduces to a minimum in steady state.

$$D = \left|\frac{P^* - P}{\Delta\omega_{VSG}}\right| \quad (27)$$

The minimum damping D_{min} used in acceleration period is constrained by VSG stability proposed in [32] as rewritten here,

$$\begin{cases} \sqrt{\dfrac{-{D_{min}}^2 + \sqrt{{D_{min}}^4 + 4J^2{c_1}^2}}{2J^2}} \le 0.1\omega_g \\ \sqrt{\dfrac{-{D_{min}}^2 + \sqrt{{D_{min}}^4 + 4J^2{c_1}^2}}{2J^2}} \le \dfrac{D_{min}}{J} \end{cases} \quad (28)$$

Note, the fulfillment of (28) ensures that the VSG inertia response is decoupled from the converter dynamics, i.e., outer voltage inner current control dynamics and LC filter dynamics. Therefore, the proposed adaptive VSG control will not experience any resonance problems.

C. Adaptive virtual inertia

The virtual inertia J only affects the VSG transient performance and further the system frequency stability. After a contingency, the inertia should be large in order to transiently output more power to reduce the system RoCoF. On the other hand, when the system returns to steady state, the inertia could be small in order to increase the damping ratio, $\zeta = D/(2\sqrt{(JH\_(dP/d\delta)}))$. Reference [26][27] proposed that the virtual inertia is chosen to be large during VSG acceleration and small during VSG deceleration. In other words, the VSG is underdamped ($\zeta < 1$) during acceleration and overdamped ($\zeta > 1$) during. However, due to the converter capacity, the virtual inertia J is limited and particularly in the underdamped situation.

In the previous section, droop and damping gain have been determined. Thus, when the VSG is accelerating (underdamped), the only unknown quantity in the overshoot calculation is the virtual inertia. In order to maximize the inertia, the overshoot can be regulated to hit the converter active power limit P_{max} exactly. Then, the virtual inertia can be computed as (29).

$$\begin{cases} PO_{P\_\omega}(J) \cdot (-\Delta\omega_{VSG}) = P_{max} - P^*, \omega_{VSG} \le \omega^* \\ PO_{P\_\omega}(J) \cdot (\Delta\omega_{VSG}) = P_{max} + P^*, \omega_{VSG} > \omega^* \end{cases} \quad (29)$$

In order to maximize the inertia, $\Delta\omega_{VSG}$ is a real-time input in (29) in order to compute virtual inertia J. Thus, at the beginning of the contingency, $\Delta\omega_{VSG}$ is small, and the virtual inertia would be very large, while at the frequency nadir, $\Delta\omega_{VSG}$ is large, the virtual inertia would be small.

Note, the transfer function G_{P_ω} in (17) considers a step change in $\Delta\omega_{VSG}$, which results in an impulse for RoCoF. The associated overshoot PO_{P_ω} approaches the maximum value P_{max} only as the RoCoF approaches infinity. In other words, the obtained virtual inertia from (29) can ensure that the power output always remains below its maximum value.

Note that, in this condition, J is a function of $R_v, X_v, D, \omega_{VSG}$. $PO_{P\_\omega}(J)$ and is highly nonlinear, as can be seen in (17). Thus, it needs some computation time to solve (29) which may make it difficult to apply (29) in a real-time control loop. Therefore, it is necessary to find the relationship between J and ω_{VSG}, while

R_v, X_v, D are the values of the parameters used during acceleration.

Taking the example for the values used in the hardware in next section, the plot of J against ω_{VSG}, computed from (29), is shown by the red line of Fig. 5, considering $\Delta\omega_{VSG}$ up to $1.5 \times 2\pi\ rad$. The obtained J is the maximum allowable virtual inertia so that the overshoot just hits the converter capacity limit.

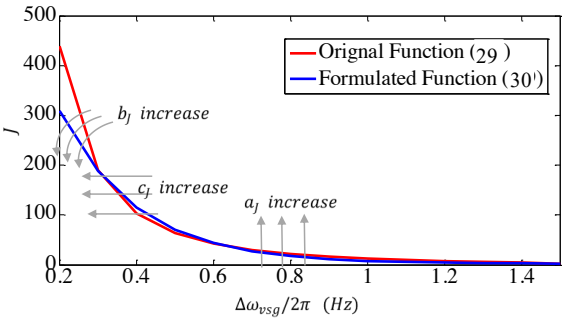

Fig. 5. Virtual inertia limits vs. frequency deviation

It can be seen from Fig. 5 that the maximum allowable virtual inertia J dramatically reduces with $\Delta\omega_{vsg}$ increase. This is because when the $\Delta\omega_{vsg}$ is low, the droop power compensation is small and there is a large space for the inertia response, so that the virtual inertia can be large. In contrast, when the $\Delta\omega_{vsg}$ is at the maximum value, taken here as 1.5 Hz, the droop power takes up the full converter rating, so that the virtual inertia should be small, and VSG works in an overdamped condition. During a contingency, $\Delta\omega_{vsg}$ increases from 0 to a certain value, and the virtual inertia reduces from large to small. At the instant of the contingency, the virtual inertia can be maximized using the proposed control.

In one way, the application of the J can be categorized according to the value of $\Delta\omega_{vsg}$. In another way, it can be formulated as a function which approximates or fits the curve (29) in Fig. 5.

$$J = \mathrm{a}_J * exp(-\mathrm{b}_J(\Delta\omega_{vsg}/2\pi + \mathrm{c}_J)) + J_{(\Delta\omega_{vsg}=max)} \quad (30)$$

When $\mathrm{a}_J = 5 \times 10^7;\ \mathrm{b}_J = 5; \mathrm{c}_J = 2.2$, the formulated function (30) is the blue line in Fig. 5, which is similar to the original function (29). The effect of the parameter a_J, b_J, c_J on the fitting function (30) are also indicated in Fig. 5. In this way, the application of (30) can achieve simultaneously varying the virtual inertia J in response to the frequency dynamics.

For the synchronous generator, the inertia time constant T_{SG}, is usually 2-6 s [35]. Similarly, when VSG is decelerating (overdamped) or in steady state, the virtual inertia could be set to give a settling time in the same range. Thus, according to (28), in steady state the virtual inertia J is constrained as (31).

$$\begin{cases} D^2 - 4JH_{dP/d\delta} \geq 0 \\ \dfrac{8J}{D} \leq T_{SG} \end{cases} \quad (31)$$

Note, in this condition, J is a function of $R_v, X_v, K_{d,0}$.

D. *Adaptive VSG control process*

Fig. 6 is used to illustrate the operation of the adaptive VSG control, where t_0 is the starting time of a new unit commitment period, t_a is the time at which the contingency happens, t_b is the time of the frequency nadir, t_1 is the settling time of the VSG, and T_p is the time of the end of this unit commitment period. Note that t_0, t_1, T_p also accords with the notation used in Fig. 4.

At the beginning, the system is stable, and VSG works in the steady-state mode. In this mode, in order to damp the generation , the damping should be set by (26); while the initial value of the virtual inertia should be small and computed from (31), where ensuring to satisfy $D^2 - 4JH_{dP/d\delta} \geq 0$, and picking the value of the J to make $\frac{8J}{D}$ approach the settled T_{SG}.

After the contingency, during $t_a - t_b$, the VSG is accelerating and a large inertia is needed to reduce the RoCoF of the system, where the damping value is first selected to ensure (28) always being satisfied in a range of virtual inertia, which is latter computed from (30). Note, this damping calculated and set down in the installation of the VSG, as well as the coefficients $\mathrm{a}_J, \mathrm{b}_J, \mathrm{c}_J$ in (30).

When the system recovers the VSG parameters are retuned for the deceleration, and during $t_b - t_1$, a large damping and small inertia are needed to suppress the oscillation. The damping now can be computed from (27), where $\Delta\omega_{VSG}$ is measured from the swing equation loop. Virtual inertia is set again according to (31). It should be noted, that the virtual inertia now is not equal to that used in the steady-state mode, because the damping value is different. The selection of the damping and virtual inertia in the steady-state mode and deceleration are done to ensure that the time constant of the inertia T_{SG} is constant.

After t_1, due to the RoCoF now being within the threshold, the VSG returns back to the steady-state mode. The values of the damping and virtual inertia now are similar to those in deceleration, but not equal to the values in the previous steady-state mode, due to the change in the power output P in (26).

The remaining energy of the ESS should cover the supplied power during the time period of this unit commitment. Thus, the selection of the droop gain is computed by (25) but constrained by (24). Table I summarizes these operations.

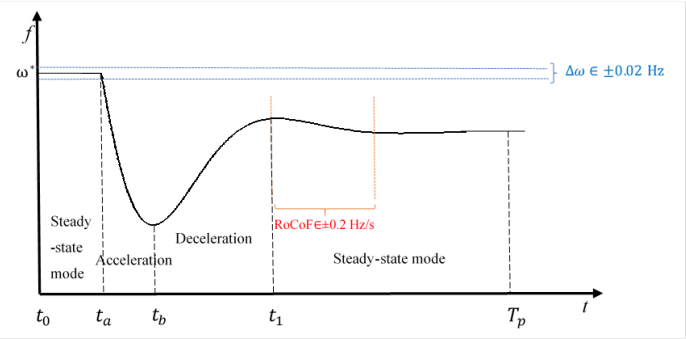

Fig. 6. Operation of adaptive VSG control

TABLE I. VSG OPERATIONS

Steady-state mode (Overdamped)	$\Delta\omega_{VSG} \in \pm 0.02$ Hz RoCoF$\in \pm 0.2$ Hz/s	Large D: (26) ; Small J: (31)
Acceleration (Underdamped)	$\Delta\omega_{VSG} * RoCoF > 0$	Small D: (28) ; Large J: (30)
Deceleration (Overdamped)	$\Delta\omega_{VSG} * RoCoF < 0$	Large D: (26) ; Small J: (31)
$K_{d,min}(0 \text{ or } D_{min}) \leq K_d(25) \leq K_{d,max}$ (24); D_{min} (28)		

IV. HARDWARE VALIDATION

The proposed adaptive control has been validated via the hardware-in-the-loop experiment and compared with the non-adaptive VSG control (fixed VSG [16-18]) and adaptive inertia & damping control (adaptive J&D [26][27]). The hardware consists of two 100 V, 2 kVA three-phase AC/DC converters as shown in Fig. 7, one is embedded VSG control while another is implemented with voltage control with adjustable frequency to emulate the grid. The structure is similar to Fig. 1, for which the parameters are given in Table II. Note, since the experiment includes only one VSG, n_d in (25) is set to be zero.

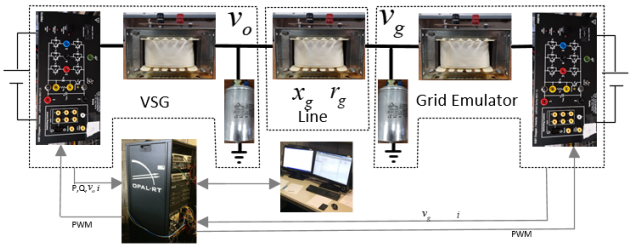

Fig. 7. Hardware experimental set-up

TABLE II. HARDWARE VSG PARAMETERS

Parameter	Value	Parameter	Value
Common parameter for different controls			
PWM/Sampling time	1350/14.81 μs	Filter inductance	0.033 H
Rated Voltage U_g	100 V	Filter resistance	0.1266 Ω
Reference voltage U^*	100 V	Filter capacitance	80 μF
Reference angular frequency ω^*	2π*50 Hz	Line inductance L_g	0.033 H
VSG reactive power droop K_q	0.01 VA/V	Line resistance R_g	1.44 Ω
Current controller P/I, K_{pc}/K_{ic}	66/339.8	Virtual inductance L_v	0.011 H
Voltage controller P/I, K_{pv}/K_{iv}	0.0535/11.987	Converter active power limit P_m	800 W
Parameter for adaptive VSG control			
Adaptive inertia	$a_J = 5 \times 10^7$; $b_J = 5$; $c_J = 2.2$	VSG time constant T_{SG}	1 s

A. Test 1: VSG control methods comparison

During frequency reduction transients, the adaptive J&D is regulated to provide large inertia in acceleration while large damping in deceleration. The paper compares the proposed method to the method in [26][27], where J=51, D=80 in acceleration, while J=2, D=100 in deceleration and J=2, D=80 in steady state. For the proposed adaptive VSG case, J is computed from (30) and D=80 in acceleration while J and D are computed from (31) and (27) in deceleration respectively, and J is computed from (31) and D is computed from (26) in steady state as given in Table I. In fixed VSG method, J=2 and D=80 keep all the time. In this test, these controls output same active power in the steady state. The grid experiences frequency drop with 0.5 Hz/s ramp from 50 Hz to 49.5 Hz at 25 s and then drop again at 27 s to 48.5 Hz.

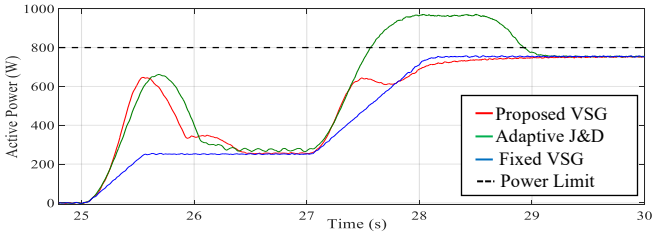

Fig. 8. Test 1 result: different VSG methods comparison

Fig. 8 depicts the results in this test. In the fixed VSG case, due to the low inertia, the VSG works in an overdamped state and droop is dominant. Thus, the VSG active power output is following the frequency variation. Although the fixed VSG does not provide large inertia, it can avoid converter overload with overdamp parameters. In contrast the adaptive J&D control can provide large inertia during the transient, but due to the fixed alternative J in acceleration, when the grid frequency further reduces to 48.5 Hz, the VSG overloads. However, the proposed adaptive VSG control considers the converter capacity and adjusts J during the transient. Consequently, it can provide inertia as large as possible during the transient while at the same time avoiding converter overload.

B. Adaptive VSG control under different RoCoF

The adaptive VSG in Test 1 (Fig. 8) does not hit the maximum power of 800 W during the acceleration. This is because the grid frequency change is relatively slow, i.e. RoCoF=0.5 Hz/s. In order to verify the effectiveness of the proposed adaptive VSG in response to various contingencies, the simulated response in obtained for a grid frequency decrease from 50 Hz to 49 Hz with RoCoF values of 0.5 Hz/s, 1 Hz/s and 2 Hz/s.

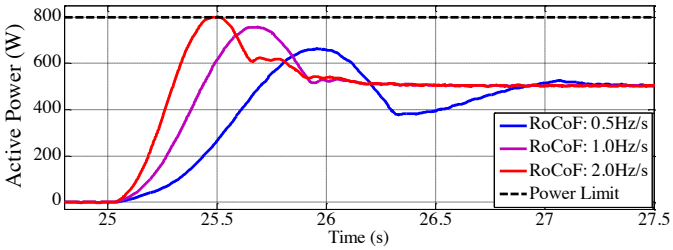

Fig. 9. Test 2 result: adaptive VSG in response to different RoCoF

Fig. 9 depicts the results from these tests. The increase in RoCoF increases the ramp rate of the power boost as would be expected and under the highest RoCoF its peak value approaches the power limit. This is consistent with the design of the adaptive virtual inertia, which is designed to achieve the maximum power when the frequency step changes. In other words, as the RoCoF approaches infinity, the peak power approaches the maximum. It can be seen that there is a power

drop in the 0.5 Hz/s RoCoF case. This is because the grid frequency does not stabilize until 27 s, while at 26 s, the virtual inertia value has adaptively decreased with the consequence that its power output becomes dominated by the droop control part.

From these tests, it can be seen that the proposed adaptive VSG control works to maximize inertia while keeping the converter output power unsaturated.

V. Case Study

The hardware experiment is an open-loop validation, for which the VSG output power has no effect on grid frequency. In any system the VSG power and grid frequency interact. Moreover, the previous validation does not account for the storage SOC limits (24) and VSG interactions as regulated by (25). In this section, we use the New England 39-bus system (see Fig. 10) with 3 wind generators (WG) (37.2% wind penetration) replacing synchronous generator to validate the proposed adaptive VSG control in a closed-loop power system and its performance with limited storage capacity. The SGs in the power system are modelled by 4th-order (two-axes) synchronous machine models. Each of the generators has both primary voltage (AVR and PSS) and frequency regulators (turbine governor). The WGs are modelled as variable-speed wind turbines with 5th-order doubly-fed induction machine models working at constant 13 m/s wind speed. The VSG is modelled using full-order Differential Algebraic Equations (13th-order), including outer voltage, inner current controls and LC filter, as detailed and verified via a hardware experiment in [19]. The VSG control is applied to the electric energy storage (ESS) which is co-located with the WG [37]. Its parameters are given in Table III. The ESS is assumed to maintain a fixed DC voltage with limited capacity and SOC, the values of which are given in each subsection. The initial power is zero, i.e. $P^* = 0, Q_0 = 0$. The dynamic data of the original 10-synchronous-generator power system can be found in [35]. and wind generators data are listed in [19]. Simulation results in this section are obtained using Dome, a Python-based power system software tool [36].

We present two scenarios. The first scenario (High SOC storage operation) aims to investigate the performance of proposed adaptive VSG installed in a single ESS compared with that of the fixed VSG in response to a system contingency. The second scenario (low SOC storage operation) simulates three ESS with adaptive VSG control or fixed VSG control considering one ESS hits the SOC limit. Both of these scenarios consider as a contingency, the loss of SG10 in Fig. 10.

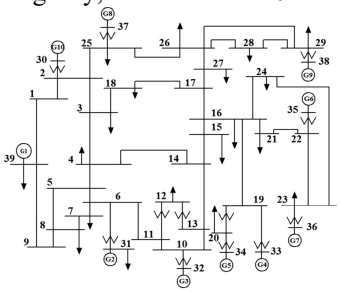

Fig. 10. New England 39-bus system

TABLE III
Power System Fixed and Adaptive VSG Settings

Parameter	Value	Parameter	Value	Parameter	Value
S_{base}	100 MVA	V_n	220 kV	K_{pv}	25
K_q	0.01	x_f	0.08 pu	K_{iv}	5
K_{pc}	20	r_f	0.01 pu	ω_f	20
K_{ic}	10	b_f	0.34 pu	x_v	0.02 pu
K_{xv}	0.01	x_g	0.08 pu	r_v	0.01 pu
T_p	80	r_g	0.005 pu	K_{ffv}	0.0

A. Scenario 1: High SOC storage operation

In this scenario, we aim to test the proposed adaptive VSG and fixed VSG controlled ESS devices, and compare their performance in normal operation. Thus, only one ESS ($n_d = 0$ in (25)) is co-located with WG1 in the system at bus 39. At 1 s, Gen 10 is lost. The maximum active power $P_m = 1.5$ pu, from (25), $K_{d,0} = 12.5$. For comparison several different virtual inertia values of J=23, J=100 and J=170 are used in the fixed VSG, while the virtual inertia is computed from (30,31) for the adaptive VSG. Fig. 11 presents the frequency. Note, the selection of the virtual inertia in the fixed VSG also takes into the consideration the maximum power limit, $P_m = 1.5$ pu. J=170 is the maximum fixed virtual inertia which maintains power output less than 1.5 pu power in relation to 2 Hz or 0.04 pu step change in grid frequency.

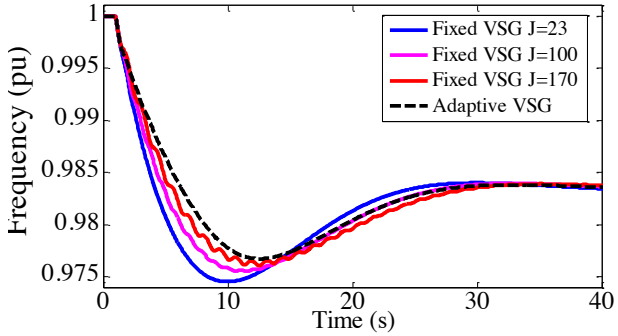

Fig. 11. Scenario 1 results: Comparison of frequency deviation for different schems under high SOC storage operation.

Comparing the frequency response under different fixed VSG scenarios from Fig. 11, it can be seen that the higher the inertia, the lower RoCoF, but the response tends to be more oscillatory with longer settling time as would be expected. In contrast, the adaptive VSG scenario has the best performance in terms of the system RoCoF and frequency nadir, meanwhile presenting little oscillation with faster stabilization than those high inertia fixed VSGs. This is because, on the one hand, at the instant of the contingency, the adaptive VSG can boost its inertia with a value which is much higher than any of the fixed VSG, which improves the RoCoF at the initial of the frequency drop as shown in Fig. 11. On the other hand, the increased damping during the deceleration helps stabilize the system faster. Note that in this case, due to the same droop gain $K_{d,0}$, being used, the steady state frequency for all scenarios ends up at the same value.

B. Scenario 2: Low SOC storage operation

In this scenario, we aim to test the proposed adaptive VSG control and fixed VSG control in low SOC storage operation.

Furthermore, to investigate the power re-scheduling (n_d in (25)) in the proposed adaptive VSG control, a second VSG controlled storage with same settings ($P_m = 1.5$ pu, $K_{d,0} = 12.5$, J=23) is implemented into the 39-bus system at bus 32 co-located with WG2 (see Fig. 10). However, in this case, one of the storages (ESS1) has low SOC with initial energy around 45 pu • s and will run out of power during the operation. The re-scheduling time T_p in (24) is down-scaled to 80 s simply to compress simulation time. Fig. 12 presents the bus-39 frequency, ESS1 energy, ESS1 active power output and ESS2 active power output.

From Fig. 12 (a), besides the conclusion obtained in scenario 1, the proposed adaptive VSG control can smooth the frequency when storage reaches its low threshold, while the fixed VSG control has a secondary frequency transient around 60 s caused by the suddenly storage turn-off, although they stabilize at the same steady state. This is because the droop gain K_d is restricted by $K_{d,max}$ in (24) and leads to a gradual reduction in droop power (see Fig. 12 (c)). Consequently, the ESS1 energy has a smooth reduction (see Fig. 12 (b)). Note, the adaptive VSG controlled ESS1 active power output steps to zero near 80 s, this is because $K_{d,max}$ becomes lower than $K_{d,min}$ and the control moves to output zero real power.

On the other hand, an increase of the droop re-scheduling gain n_d can improve the system frequency (see Fig. 12 (a) broken-line) in steady state. This is owing to the high SOC ESS compensating more power as shown in Fig. 12 (d).

In reality, T_p is 20 min and if more ESS are involved in the proposed adaptive VSG control, the frequency reduction gradient, caused by the low SOC storage re-scheduling, can be much lower.

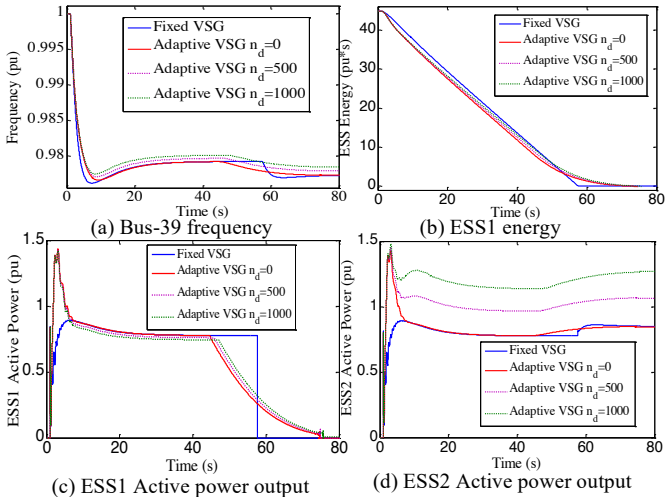

(a) Bus-39 frequency (b) ESS1 energy

(c) ESS1 Active power output (d) ESS2 Active power output

Fig. 12: Scenario 2 results: Low SOC storage operation.

VI. Conclusion

The paper proposed an adaptive VSG control considering the storage and converter capacity. The control can maximize the inertia in order to reduce RoCoF and frequency nadir meanwhile keeping the converter unsaturated. Moreover, the power re-scheduling method can utilize ESS optimally and avoid the extra transient caused by the storage offline. Although the control introduced in paper is adaptive, the constraints imposed by the rating and SoC of the ESS can also be used to select the parameters for the fixed VSG.

References

[1] F. M. Uriarte, C. Smith, S. Vanbroekhoven, and R. E. Hebner, "Microgrid Ramp Rates and the Inertial Stability Margin," IEEE Trans. Power Syst., 2015.

[2] F. Milano, F. Dorfler, G. Hug, D. J. Hill, and G. Verbič, "Foundations and challenges of low-inertia systems (Invited Paper)," in 20th Power Systems Computation Conference, PSCC 2018, 2018.

[3] V. Knap, S. K. Chaudhary, D. I. Stroe, M. Swierczynski, B. I. Craciun, and R. Teodorescu, "Sizing of an energy storage system for grid inertial response and primary frequency reserve," IEEE Trans. Power Syst., 2016.

[4] H. P. Beck and R. Hesse, "Virtual synchronous machine," 2007 9th Int. Conf. Electr. Power Qual. Util. EPQU, 2007.

[5] J. Fang, Y. Tang, H. Li, and X. Li, "A Battery/Ultracapacitor Hybrid Energy Storage System for Implementing the Power Management of Virtual Synchronous Generators," IEEE Trans. Power Electron., 2018.

[6] Y. Ma, W. Cao, L. Yang, F. F. Wang, and L. M. Tolbert, "Virtual Synchronous Generator Control of Full Converter Wind Turbines with Short-Term Energy Storage," IEEE Trans. Ind. Electron., 2017.

[7] J. Rocabert, A. Luna, F. Blaabjerg, and P. Rodríguez, "Control of power converters in AC microgrids," IEEE Trans. Power Electron., vol. 27, no. 11, pp. 4734–4749, 2012.

[8] M. Yu et al., "Instantaneous penetration level limits of nonsynchronous devices in the British power system," IET Renew. Power Gener., 2017.

[9] D. Duckwitz and B. Fischer, "Modeling and Design of df/dt -Based Inertia Control for Power Converters," IEEE J. Emerg. Sel. Top. Power Electron., 2017.

[10] S. Khan, B. Bletterie, A. Anta, and W. Gawlik, "On small signal frequency stability under virtual inertia and the role of PLLs," Energies, 2018.

[11] U. Tamrakar, D. Galipeau, R. Tonkoski, and I. Tamrakar, "Improving transient stability of photovoltaic-hydro microgrids using virtual synchronous machines," 2015 IEEE Eindhoven PowerTech, PowerTech 2015, pp. 1–6, 2015.

[12] C. Sun, J. N. Paquin, F. Al Jajeh, G. Joos, and F. Bouffard, "Implementation and CHIL Testing of a Microgrid Control System," in 2018 IEEE Energy Conversion Congress and Exposition, ECCE 2018, 2018.

[13] B. K. Poolla, D. Groß, and F. Dörfler, "Placement and Implementation of Grid-Forming and Grid-Following Virtual Inertia and Fast Frequency Response," IEEE Trans. Power Syst., vol. 34, no. 4, pp. 3035–3046, 2019.

[14] European Network of Transmission System Operators for Electricity, "High Penetration of Power Electronic Interfaced Power Sources (HPoPEIPS)," ENTSO-E Guid. Doc. Natl. Implement. Netw. codes grid Connect., vol. 29, no. March, 2017.

[15] J. L. R. T. E. R. Z. A. A. P. S. P. N. K. N. F. M. van der M. V. S. M. N. A. K. S. R. T. Hennig, "Deliverable D1.5 Power system risk analysis and mitigation measures," MIGRATE, vol. Sep, no. 15, 2019.

[16] Q. C. Zhong, "Virtual Synchronous Machines: A unified interface for grid integration," IEEE Power Electron. Mag., 2016.

[17] S. D'Arco, J. A. Suul, and O. B. Fosso, "A Virtual Synchronous Machine implementation for distributed control of power converters in SmartGrids," Electr. Power Syst. Res., 2015.

[18] J. Liu, Y. Miura, and T. Ise, "Comparison of Dynamic Characteristics between Virtual Synchronous Generator and Droop Control in Inverter-Based Distributed Generators," in IEEE Transactions on Power Electronics, 2016.

[19] J. Chen, M. Liu, C. Oloughlin, F. Milano, and T. Odonnell, "Modelling, simulation and hardware-in-the-loop validation of virtual synchronous generator control in low inertia power system," in 20th Power Systems Computation Conference, PSCC 2018, 2018.

[20] Z. Shuai, Y. Hu, Y. Peng, C. Tu, and Z. J. Shen, "Dynamic Stability Analysis of Synchronverter-Dominated Microgrid Based on Bifurcation Theory," IEEE Trans. Ind. Electron., 2017.

[21] K. Shi, W. Song, P. Xu, R. Liu, Z. Fang, and Y. Ji, "Low-Voltage Ride-Through Control Strategy for a Virtual Synchronous Generator Based on Smooth Switching," IEEE Access, 2017.

[22] K. Shi, H. Ye, P. Xu, D. Zhao, and L. Jiao, "Low-voltage ride through

control strategy of virtual synchronous generator based on the analysis of excitation state," IET Gener. Transm. Distrib., 2018.
[23] J. Chen; M. Liu; T. O'Donnell, "Replacement of Synchronous Generator by Virtual Synchronous Generator in the Conventional Power System," 2019 IEEE PES Gen. Meet., vol. Atlanta, US, 2019.
[24] H. Wu et al., "Small-Signal Modeling and Parameters Design for Virtual Synchronous Generators," IEEE Trans. Ind. Electron., 2016.
[25] J. Alipoor, Y. Miura, and T. Ise, "Power system stabilization using virtual synchronous generator with alternating moment of inertia," IEEE J. Emerg. Sel. Top. Power Electron., 2015.
[26] D. Li, Q. Zhu, S. Lin, and X. Y. Bian, "A Self-Adaptive Inertia and Damping Combination Control of VSG to Support Frequency Stability," IEEE Trans. Energy Convers., 2017.
[27] F. Wang, L. Zhang, X. Feng, and H. Guo, "An Adaptive Control Strategy for Virtual Synchronous Generator," IEEE Trans. Ind. Appl., 2018.
[28] L. Torres, C. Espinoza, V. Hertem, and S. E. Reviews, "Self-tuning virtual synchronous machine : A control strategy for energy storage systems to support dynamic frequency control A Virtual Synchronous Machine implementation for distributed control of power converters in SmartGrids The relevance of inertia in," vol. 29, no. 2016, pp. 999–1009, 2018.
[29] U. Markovic, Z. Chu, P. Aristidou, and G. Hug, "LQR-Based Adaptive Virtual Synchronous Machine for Power Systems With High Inverter Penetration," IEEE Trans. Sustain. Energy, 2019.
[30] W. Fan, X. Yan, and T. Hua, "Adaptive parameter control strategy of VSG for improving system transient stability," in 2017 IEEE 3rd International Future Energy Electronics Conference and ECCE Asia, IFEEC - ECCE Asia 2017, 2017.
[31] X. Hou, Y. Sun, X. Zhang, J. Lu, P. Wang, and J. M. Guerrero, "Improvement of Frequency Regulation in VSG-Based AC Microgrid via Adaptive Virtual Inertia," IEEE Trans. Power Electron., 2019.
[32] J. Chen and T. O'Donnell, "Parameter constraints for virtual synchronous generator considering stability," IEEE Trans. Power Syst., 2019.
[33] J. Chen; T. O'Donnell, "Analysis of virtual synchronous generator control and its response based on transfer functions," IET Power Electron., vol. 12, no. 11, pp. 2965–2977, 2019.
[34] EIRGRID and SONI, "RoCoF Alternative & Complementary Solutions Project."
[35] F. Milano, "Power system modelling and scripting," Power Syst., 2010.
[36] F. Milano, "A python-based software tool for power system analysis," in IEEE Power and Energy Society General Meeting, 2013.
[37] M. G. Taul, X. Wang, P. Davari, and F. Blaabjerg, "An Overview of Assessment Methods for Synchronization Stability of Grid-Connected Converters under Severe Symmetrical Grid Faults," IEEE Trans. Power Electron., 2019.
[38] J. Chen, M. Liu, F. Milano and T. O'Donnell, "Placement of Virtual Synchronous Generator Controlled Electric Storage combined with Renewable Generation," *2019 IEEE Milan PowerTech*, Milan, Italy, 2019, pp. 1-6.